

The static and dynamic shear-tension mechanical response of AM Ti6Al4V containing spherical and prolate voids



Rafael Fadida^{a,*}, Amnon Shirizly^a, Daniel Rittel^b

^a POB 2250, Haifa, 3102102, Israel

^b Faculty of Mechanical Engineering, Technion, 3200003, Haifa, Israel

ARTICLE INFO

Article history:

Received 3 March 2019

Revised 23 May 2019

Accepted 23 May 2019

Keywords:

Additive manufacturing

Ti6Al4V

Artificial porosity

Spherical

Prolate

Dynamic shear behavior

ABSTRACT

The dynamic tensile response of additively manufactured Ti6Al4V shear-tension specimens containing discrete artificial pores was investigated under quasi-static and dynamic loading. Specimens containing spherical and spheroidal pores were designed with one or three pores, whose total volume fraction was kept equal to that of the single pore, albeit with variable spacing between the pores. Specimens containing prolate pores were designed with different pore orientations with respect to the shear direction. For the geometrical configurations investigated, it was found that the very presence of the pore (or pores) reduces the displacement to failure, compared to the dense specimens, in both quasi-static and dynamic regimes. The shape of the pore, the number of pores and their distribution, have a minor effect on results, in both loading-rate regimes. Similarly, there is no sensitivity to the orientation of the prolate pore, for the investigated spheroid and gauge dimensions.

© 2019 Published by Elsevier Ltd.

1. Introduction

Metal additive manufacturing (AM) processes allows the construction of 3D components according to a layer-by-layer method. One of the common AM methods is the powder bed fusion (PBF), which creates solid parts by selective melting of powder layers repeatedly using a thermal energy source (ISO/ASTM International, 2015). The manufacturing process begins with a digital model file created from a CAD program. The file is converted into industry standard file format (usually STL file) and then into machine language (G-code) using dedicated slicing software, which divide it to a stack of horizontal flat slices. Next, a high power energy source, such as laser or electron beam is used to melt a thin layer of powder according to the regions represents solid in the first slice of the part. Afterwards, the part is slightly lowered, a new layer of powder is applied and the process repeats itself until the part is complete. In the last years, studies have shown that laser-based (or electron beam) additive manufacturing processes, can fabricate dense Ti6Al4V titanium alloy with strength properties (i.e., yield strength or ultimate tensile strength) comparable or even superior to those of conventional wrought material (Becker, Beck, & Scheffer, 2015; Beibei et al., 2018; Facchini et al., 2010; Hutasoit, Masood, Pogula, Shuva, & Rhamdhani, 2018; Ladani, Razmi, & Choudhury, 2014; Machry et al., 2016; Moletsane et al., 2016; Tong, Bowen, Persson, & Plummer, 2017). Not only dense, but even porous materials can be fabricated with an internal pores network adjusted to the desired application. For example orthopedic or dental implants can be designed with an elastic modulus, which is closer to that of the bone, in

* Corresponding author.

E-mail address: fadidarafi@gmail.com (R. Fadida).

order to avoid stress shielding effects (Wang et al., 2016; Wauthle et al., 2015). The effect of porosity on plastic deformation, damage and rupture has been subjected to extensive studies in the literature, most of them analytical or numerical. Since the seminal model of Gurson (1977), which analyzes plastic flow in a porous medium, the well-known ductile fracture mechanism, characterized by the growth and coalescence of voids has been successively studied (Benzerga, 2002; Gologanu, Leblond, & Devaux, 1993; Koplik & Needleman, 1988; Li & Steinmann, 2006; Tvergaard, 1982), mostly at high triaxialities. Barsoum and Faleskog (2007a), showed numerically that the presence of pre-existing voids has no significant contribution to the onset of fracture at low level of triaxiality. They suggest that shear failure can be predicted by simple criterion based on a critical shear deformation value. An extension of Gurson model that incorporates damage growth in shear-dominated stress state was suggested by Nahshon and Hutchinson (2008). Numerical studies deal with the behavior of voids under shear were presented by Tvergaard (2008) for cylindrical voids, by Nielsen, Dahl, and Tvergaard (2012) for spherical voids, and by Scheyvaerts, Onck, Tekoğlu, and Pardoën (2011) for ellipsoidal voids. The lack of appropriate technology to fabricate 3D voids has essentially favored mainly analytical and numerical studies. With additive manufacturing technology, the combination of mechanical properties, which are comparable to wrought material and the ability to fabricate artificial internal porosity, opens a door for innovative experimental studies that can relate between the pores' properties (e.g., geometry, volume fraction) and the mechanical behavior of the material. Additive manufacturing can therefore enrich existing analytical models dealing with the effect of porosity on plasticity. Recently, Andreau et al. (2017) presented some key rules for the fabrication of artificial spherical pores within additively manufactured 316L stainless steel samples. Wilson-Heid, Novak, and Beese (2018) investigated the effect of internal pre-existing penny-shaped pores on the tensile strength of 316L fabricated by L-PBF (Laser Powder Bed Fusion). They found that the presence of pore did not affect elongation to failure or strength until the pore diameter exceeds 600 μm , which is 0.1 times the specimen gauge diameter.

It is well established that the strength of most metals and alloys increases with the strain rate (strain-rate sensitivity) (Blazynski, 1987). It is therefore, necessary to design or numerically simulate mechanical components according to the mechanical properties at the relevant strain rates (Nicholas, 1981) particularly when those are high. While the dynamic behavior of wrought titanium is well documented in the literature (Nicholas, 1980; Wulf, 1979) the behavior of additively manufactured titanium at high strain rates has only been investigated by a few researchers (Jones et al., 2016; Matthes et al., 2017). Moreover, publications concerning porous materials fabricated by additive manufacturing, and subjected to dynamic loading, are still quite scarce (Biswas, Ding, Balla, Field, & Bandyopadhyay, 2012). Fadida, Shirizly, and Rittel (2015, 2018) showed that the strength properties in compression and tension of AM Ti6Al4V, in both quasi-static and dynamic regimes, are comparable, or even higher, than those of the wrought material. In addition, it was demonstrated consistently that the material properties are significantly reduced due to the presence of artificial internal spherical voids. The Ti6Al4V alloy (wrought or AM) is known to have a limited strain hardening capacity (de Formanoir et al., 2017; Fadida et al., 2015), in this context, Sevostianov and Kachanov (2001) suggest a yield condition for porous material that reflect the shape and orientation of pores for perfectly plastic material. Their study is based on experimental observation e.g., (da Silva & Ramesh, 1991) that shows that the strain at the onset of yield is relatively insensitive to the void volume fraction up to a level of app. 20%. Zohdi, Kachanov, and Sevostianov (2002) show numerical simulations that support these observations. Since McClintock (1968), Rice and Tracey (1969), Hancock and Mackenzie (1976) and many others, the stress triaxiality (the ratio of hydrostatic stress to the von Mises equivalent stress - t_r) was shown to have a significant effect on ductility. It is generally agreed that at high level of triaxiality the equivalent strain to fracture decreases with increasing stress triaxiality (Danas & Ponte Castaneda, 2012). However, the stress triaxiality is insufficient by itself to characterize the stress state in ductile failure. According to Bao and Wierzbicki (2004), none of the models introducing fracture criteria gives a consistent results over the entire triaxiality range. By contrast, the Lode parameter (the third invariant of the deviatoric stress tensor - μ) plays a significant role in ductile failure, especially at low values of stress triaxiality (Xiaosheng et al., 2011; Xiaosheng and Jinkook, 2006). Barsoum and Faleskog (2007b), experimentally determined the ductility of several alloy steels over a wide range of triaxialities and Lode parameter using a specimen loaded in combined tension and torsion. They showed that the rupture mechanism changes from internal necking to shearing between voids as a function of both stress triaxiality and Lode parameter. Therefore, the behavior of materials over a wide range of triaxialities and Lode parameter is required for accurate simulations. Finally, one should mention the work of Molinari and Mercier (2001) who showed that micro-inertia has a significant role in the process of failure at high strain rate loadings combined with low strain rate sensitivity. Micro-inertia has been shown to delay the void volume change. The shear-tension specimen (STS) developed by Dorogoy and Rittel (2005b,a) is quite convenient among other specimens. The unique geometry of the STS enforces a stress state within the specimen's gauge section between generalized tension ($\mu = -1$) and generalized shear ($\mu = 0$), which is approximately -0.5 . A data reduction technique specially developed allows reduce the measured load-displacement ($P-d$) data into the material's stress strain curve, i.e., average Mises stress against average equivalent plastic strain ($\hat{\sigma}_M - \hat{\varepsilon}_p$). A detailed numerical study due to Dorogoy and Rittel (2017); Dorogoy, Rittel, and Godinger (2015, 2016) show that the calculated $\hat{\sigma}_M - \hat{\varepsilon}_p$ represents correctly the material true stress-strain curve. As mentioned above, the subject of shear loading and (artificial) porosity has not been addressed extensively from an experimental standpoint, in both the quasi-static and dynamic loading regimes. Therefore, the present study reports on the effect of discrete artificial spherical and spheroidal pores within additively manufactured specimens, in which a combined shear and tension stress state is imposed, at different strain rates.

This paper is organized as follows. Section 2 describes the experimental technique and specimens' design. Section 3 presents the experimental results. Section 4 discusses in the experimental results, followed by Section 5 for summary and conclusions.

2. Materials and methods

2.1. Dynamic tension tests

The Split Hopkinson (Kolsky) tensile bar (SHTB) is a well-known experimental technique to characterize the tensile properties of materials at high strain rates (10^2 – 10^4 s⁻¹). The experimental principal and the test apparatus were first introduced by Kolsky (1949) for compression, and further developed by Harding, Wood, and Campbell (1960). In the tension apparatus the specimen is threaded to be inserted into the two long bars, made of hardened C300 maraging steel. The tensile pulse is generated by shooting a hollow striker tube against a flange ending the incident bar. The stress waves are measured by means of strain gauges cemented at mid-length of the incident and transmitted bars. The three strain pulses that are measured are incident, reflected and transmitted. The forces on both sides of the specimen are calculated based on the measured strains and verified for dynamic equilibrium. The resulting stress-strain curve is deemed to be valid if dynamic force equilibrium is achieved (see also Rotbaum & Rittel, 2014). The forces in the incident and the transmitted bars are given by:

$$F_{in} = A_b E_b (\varepsilon_i + \varepsilon_r) \quad (2.1.1)$$

$$F_{out} = A_b E_b \varepsilon_t \quad (2.1.2)$$

Where, A_b is the cross section area of the bar, E_b is the Young's modulus of the bar and ε_i , ε_r , ε_t are the incident, reflected and transmitted strains respectively.

As mentioned, equilibrium is fulfilled when

$$F_{in} = F_{out} \quad (2.1.3)$$

Further development of equations can be found in many literature sources, see e.g., (George T. (Rusty) Gray, 2000; Weinong W. Chen, 2011).

2.2. Specimen design and manufacturing

2.2.1. Shear-tension specimen design

The shear-tension specimen (STS) geometry consists of a cylinder having an inclined gauge section created by two diametrically opposed semi-circular slots, which are machined at 45° with respect to the longitudinal axis. This unique geometry creates a narrow gauge section, within which a shear deformation mode is dominant. This design was originally developed by Rittel, Lee, and Ravichandran (2002) for testing materials under combined shear-compression (SCS) stress state. The specimen was thoroughly investigated under quasi-static and dynamic loading by Dorogoy and Rittel (2005b,a). Later, the specimen geometry was adjusted for shear-tension loading by adding threads on both sides of the cylinder. The shear-tension design was successively investigated, experimentally and numerically by Dorogoy and Rittel (2017) and Dorogoy et al. (2015, 2016).

2.2.2. Dense STS manufacturing

The fully dense Ti6Al4V was additively manufactured using the DMLS™ process, which uses a high power laser source in an argon-filled chamber to melt the powdery raw material. As described, in the end of the fabrication process a fully dense solid part is obtained. A series of cylindrical rods were fabricated and then were lathe-machined and milled by CNC to the final geometry (Fig. 1). The outer surface of the cylinder was left untouched. The dimensions of the specimen's gauge

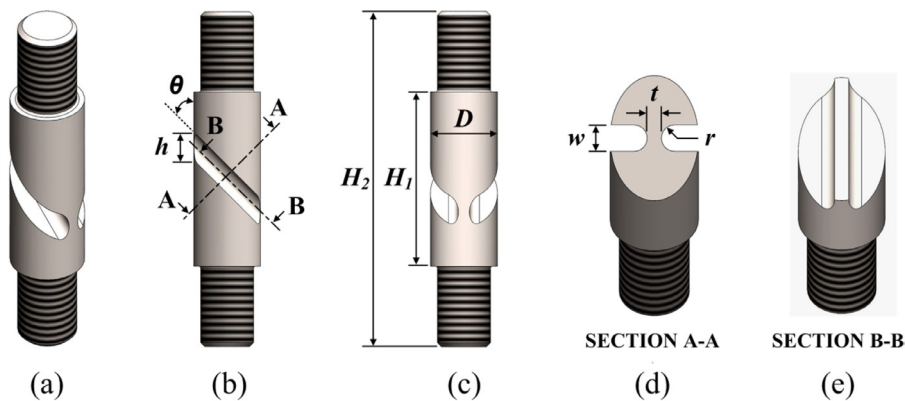


Fig. 1. A shear-tension specimen geometry: (a) Isometric projection, (b) Front view, (c) Side view, (d) Section view (A-A) perpendicular to the gauge inclination and (e) Section view B-B parallel to the gauge inclination, which represents the mid-section of the gauge.

Table 1

The geometrical dimensions of the shear-tension specimen, which are common to all types of specimen in the present study.

| Dimensions | H ₂ | H ₁ | D | h | w | t | r | θ |
|------------|----------------|----------------|----|------|---|-----|-----|-----|
| Value [mm] | 50 | 26 | 10 | 4.24 | 3 | 1.6 | 1.5 | 45° |

section, based on Dorogoy et al. (2016), and described in Table 1. The threads on of both sides of the specimen are 5/16 UNF with 12 mm length. The specimens were designed to be almost identical in their geometrical dimensions. The typical tolerance for specimen's gauge section dimensions (Fig. 1d) were of the order of ± 0.1 mm.

2.2.3. STS with spherical pores

It was recently experienced that embedded artificial pores of almost any shape can be fabricated down to a diameter (or other characteristic dimension) of $\varnothing 300$ μm (Fadida et al., 2018). In that work, the pores were deliberately embedded into a tensile specimen to explore their influence on the mechanical response of the specimen. It is clear that when the diameter of the pore is relatively small compared to the specimen's gauge the pore's effect on the mechanical response is expected to be negligible. It was found that the critical ratio between the pore diameter and specimen's gauge diameter, above which the pore existence influences the mechanical behavior, is 0.15. In fact, the smallest pore size, which has significant effect, was identified as $\varnothing 600$ μm and the specimen's gauge diameter was $\varnothing 4$ mm. Hence in the present study, spherical pores above 600 μm in diameter were chosen for tests. Three types of specimens with embedded spherical pores were fabricated according to the CAD model (i.e., an inner cavity in the CAD model generates, in practice, a non-molten void in the laser-processed part). The first specimen type contains a single pore, 650 μm in diameter (d) located at the geometric center of the specimen gauge. The second type contains $3 \times \varnothing 450$ μm pores, lined up along the specimen's gauge and the distance (L) between each pore to the other is 2 mm. The ratio of the distance between the pores centers to the pore radius is nearly 9. The total volume of the three pores was set to be equal to the volume of the single $\varnothing 650$ μm pore. The third type is similar to the second type but, the distance between each pore was set to 4 mm. Fig. 2 illustrates the pores arrangement inside the shear-tension specimens and Table 2 summarizes the pores' geometric properties.

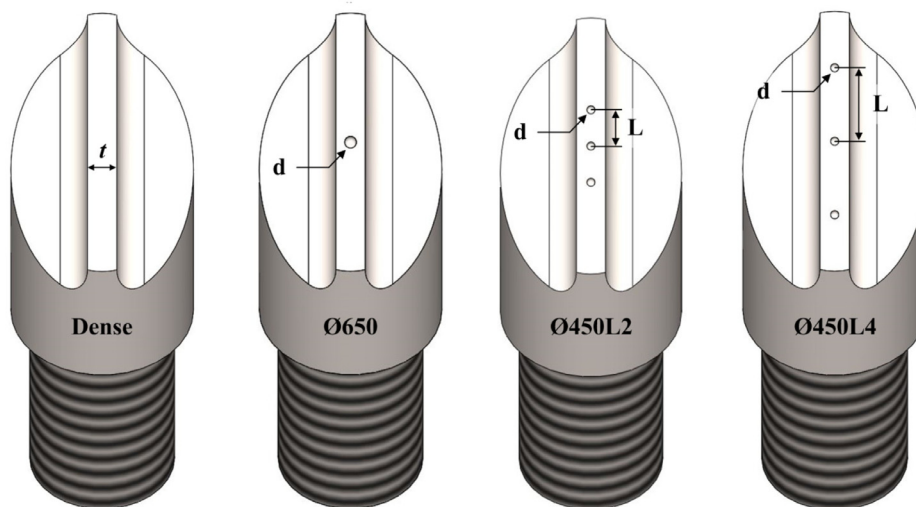


Fig. 2. A cross-section view of the specimen's CAD model at the middle of the gauge. Types of specimens, from left to right: Dense, Ø650, Ø450L2 and Ø450L4.

Table 2

Summary of the geometrical properties of the specimens contains internal spherical pores.

| Specimen type | Dense | Ø650 | Ø450L2 | Ø450L4 |
|--------------------------------------|-------|-------|----------|-----------|
| Number of artificial pores | 0 | 1 | 3 | 3 |
| Pore diameter, d [μm] | – | 650 | 450 | 450 |
| Distance between pores, L [mm] | – | – | 2 | 4 |
| Pore total volume [mm^3] | – | 0.143 | 0.143 | 0.143 |
| $L / (d/2)$ ratio | – | – | ~ 9 | ~ 18 |

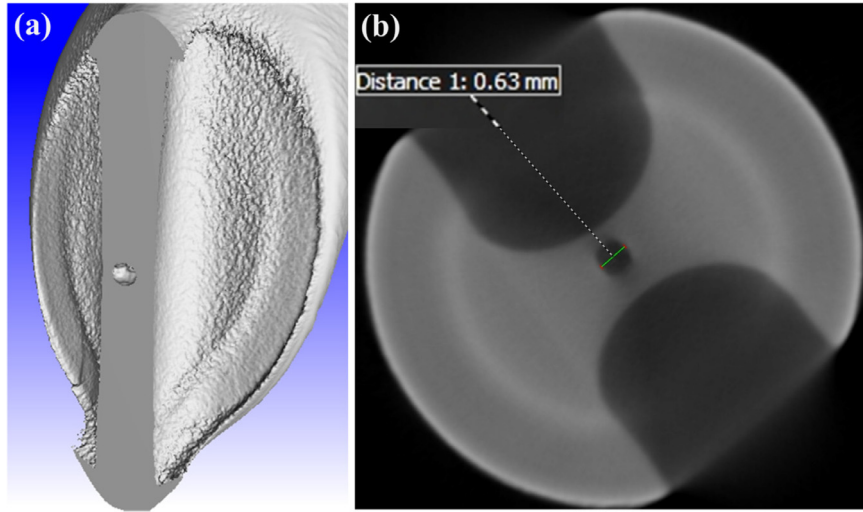


Fig. 3. A CT images of the specimen contains $\varnothing 650 \mu\text{m}$ pore (a) and its measured diameter (b).

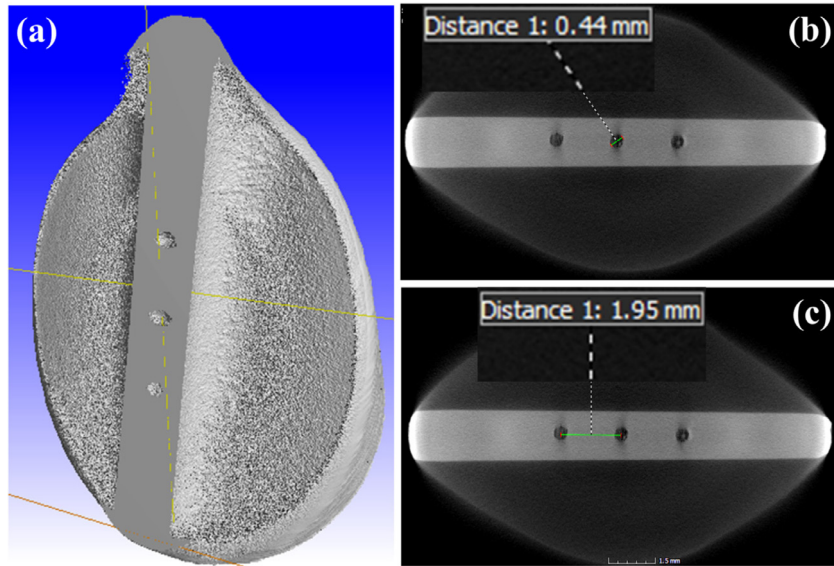


Fig. 4. A CT images of the specimen contains $3 \times \varnothing 450 \mu\text{m}$ pores (a). Typical measured values of the pore diameter (b) and the distance between two adjacent pores (c).

Fig. 3 shows CT images of two specimen types, the one that contain a single $\varnothing 650 \mu\text{m}$ pore located at the geometric center of the specimen, and the other containing $3 \times \varnothing 450 \mu\text{m}$ pores, located 2 mm apart from each other. The CT scans highlight the good quality of the additive manufacturing process, where all measurements of spherical pore diameter or distance between spherical pores were kept within tolerance of $\pm 0.05 \text{ mm}$, compared to the CAD model. Visual impression of CT scans reveal that the $\varnothing 650 \mu\text{m}$ pore shape is quite similar to ideal sphere, characterized by an inner bumpy surface, while the shape of the $\varnothing 450 \mu\text{m}$ pores seems a little less spherical. It should be noted that the surface roughness and the geometrical accuracy of the part lies within the range of the powder grain size (EOS GmBH, 2004). In the current study, a $20 \mu\text{m}$ powder grain size was used, which expected to yield $\pm 0.05 \text{ mm}$ accuracy.

2.2.4. STS with prolate spheroidal pores

A set of specimens were manufactured with a prolate spheroidal pores. The ratio between the major axis (C), and the minor axis (A) of the ellipse was set to $b_e C/A = 3$, and $A = 450 \mu\text{m}$. The prolate pore was located at the geometric center of the gauge so its major axis was aligned with the gauge mid-section. The volume of the prolate pore was set to be equal to the volume of the $\varnothing 650 \mu\text{m}$ spherical pore (or equal to the total volume of $3 \times \varnothing 450 \mu\text{m}$ pores). 4 types of specimens were fabricated, in which the angle of the elongated pore was systematically rotated with respect to the mid-section of the

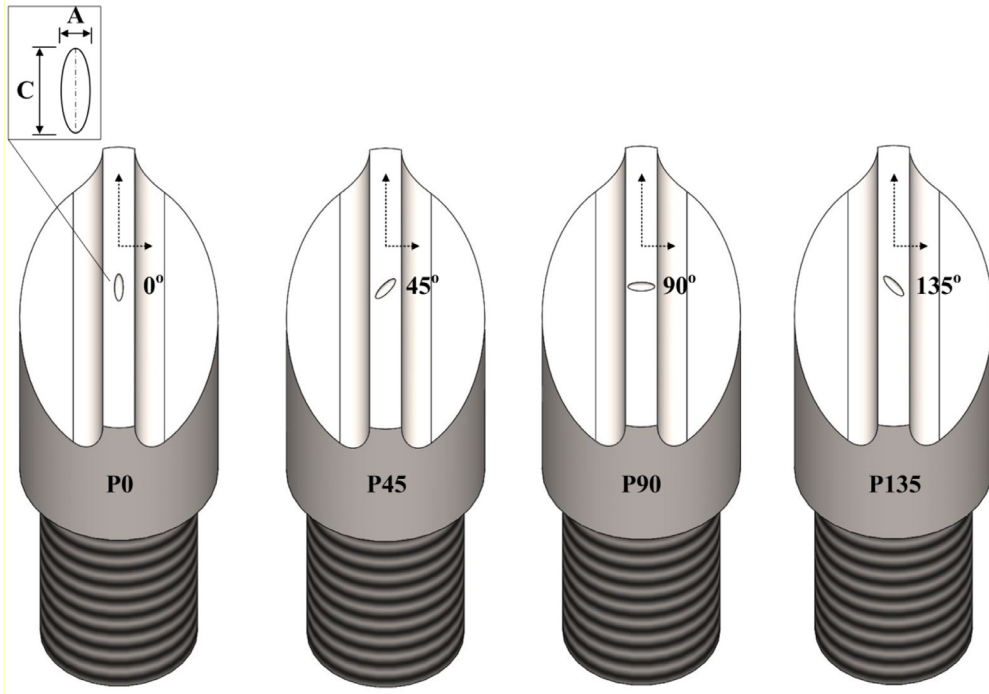


Fig. 5. A cross section view of the CAD model at the middle of the gauge. Types of specimens from left to right: P0, P45, P90 and P135.

Table 3

Summary of the geometrical properties of the specimens contains internal spheroid pore.

| Specimen type | P0 | P45 | P90 | P135 |
|--|-------|-------|-------|-------|
| Number of artificial pores | 1 | 1 | 1 | 1 |
| Pore minor diameter, A [μm] | 450 | 450 | 450 | 450 |
| Pore major diameter, C [μm] | 1350 | 1350 | 1350 | 1350 |
| Pore orientation | 0° | 45° | 90° | 135° |
| Pore total volume [mm^3] | 0.143 | 0.143 | 0.143 | 0.143 |

specimen gauge, by an angle of 0°, 45°, 90° and 135°, as illustrated in Fig. 5 and summarized in Table 3. Fig. 6 shows CT images of specimen containing a single prolate pore located at the geometric center of the specimen.

2.2.5. Void volume fraction

All the pore containing specimens were set to be with the same void volume fraction. The following calculations show the volume of the pore (or pores) and the volume of the specimen gauge.

The volume of single spherical pore, where $d = 650 \mu\text{m}$:

$$V_1 = \frac{4\pi}{3} \left(\frac{d}{2} \right)^3 = 0.143 [\text{mm}^3]$$

The total volume of three spherical pores, where $d = 450 \mu\text{m}$:

$$V_2 = 0.143 [\text{mm}^3]$$

The volume of prolate pore, where $A = 450$ and $C = 1350 \mu\text{m}$:

$$V_3 = \frac{4\pi}{3} \left(\frac{A}{2} \right)^2 \left(\frac{C}{2} \right) = 0.143 [\text{mm}^3]$$

The volume of the gauge section:

$$V_{\text{gauge}} = [(2r + t) \cdot w) - (\pi \cdot r^2)] \cdot (D / \cos(\theta)) \cong 95.2 [\text{mm}^3]$$

All pore configurations have the same volume:

$$V_1 = V_2 = V_3 = V_{\text{void}}$$

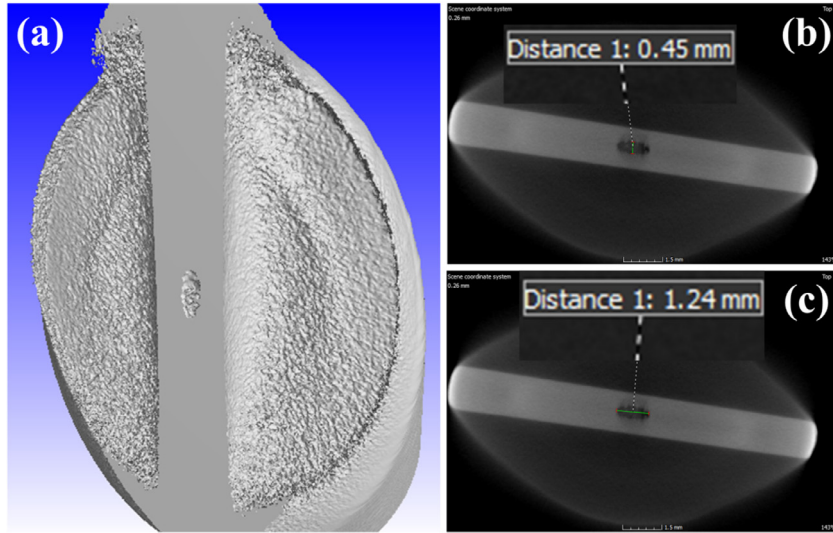


Fig. 6. A CT images of the specimen contains prolate pore ($450 \times 1350 \mu\text{m}$) at angle of 0° . (a). Typical measured values of the pore dimensions (b and c).

The void volume fraction:

$$f = \frac{V_{\text{void}}}{V_{\text{gauge}}} = 0.0015 = 0.15\%$$

3. Results

3.1. Quasi-static tension of STS with spherical pores

Consistent with our previous work (Fadida et al., 2018), we will report here macroscopic load-displacement characteristics of geometrically identical specimens, in order to avoid complications related to the stress concentration around the voids that precludes reporting homogeneous stress-strain values (Bourcier, Koss, Smelser, & Richmond, 1986). Quasi-static tensile testing was performed to measure the load-displacement of the fully dense additively manufactured STS and compare it to the pore-containing specimens. A set of 4 specimens of each type, labelled as Dense, Ø650, Ø450L2 and Ø450L4, were tested in tension on a servo-hydraulic MTS machine at a nominal strain rate of $1 \times 10^{-4} \text{ s}^{-1}$. The vertical displacements were recorded using an optical laser extensometer, while force values were obtained from the machine load cell. Fig. 7 (a–d) shows the load-displacement results of the 4 specimen types. The red thick line represents the mean curve of 4 specimens and the black dotted lines represent the minimum and maximum curves to illustrate the level of experimental dispersion of the results. Fig. 8 summarizes the load-displacement results of all mean curves of all specimen types that presented in Fig. 7 (a–d). A slight reduction in the displacement to failure can be observed in specimens containing pores compared to the dense specimens, while changes in load can barely be observed. Note that up to displacement of approx. 0.2 mm the mechanical response of all specimen types is quite similar.

3.2. Dynamic tension of STS with spherical pores

The geometry of the specimens and pores arrangements in the dynamic tests is identical to that used for the quasi-static tests. A set of 5 specimens of each specimen type were tested using the split Hopkinson tensile bar (SHTB). Fig. 9 (a–d) shows the load-displacement results of the fully dense specimens (i.e., Dense) and the specimens containing pores (i.e., Ø650, Ø450L2 and Ø450L4). Fig. 10 summarizes the load-displacement results of all mean curves of all specimen types that presented in Fig. 9 (a–d). Similar to the quasi-static results, the displacement to failure of the specimens containing spherical pores is smaller than that of the dense specimens while the differences in load are again quite minor. It can be observed that the mechanical response of the specimen types containing pore (or pores) is quite similar. The strain rate was determined according to the average equivalent plastic strain on the mid-section of the gauge versus time and it is approximately $1 \times 10^4 \text{ s}^{-1}$. For further information on the calculation procedure of the strain rate, the reader is referred to the appendix section.

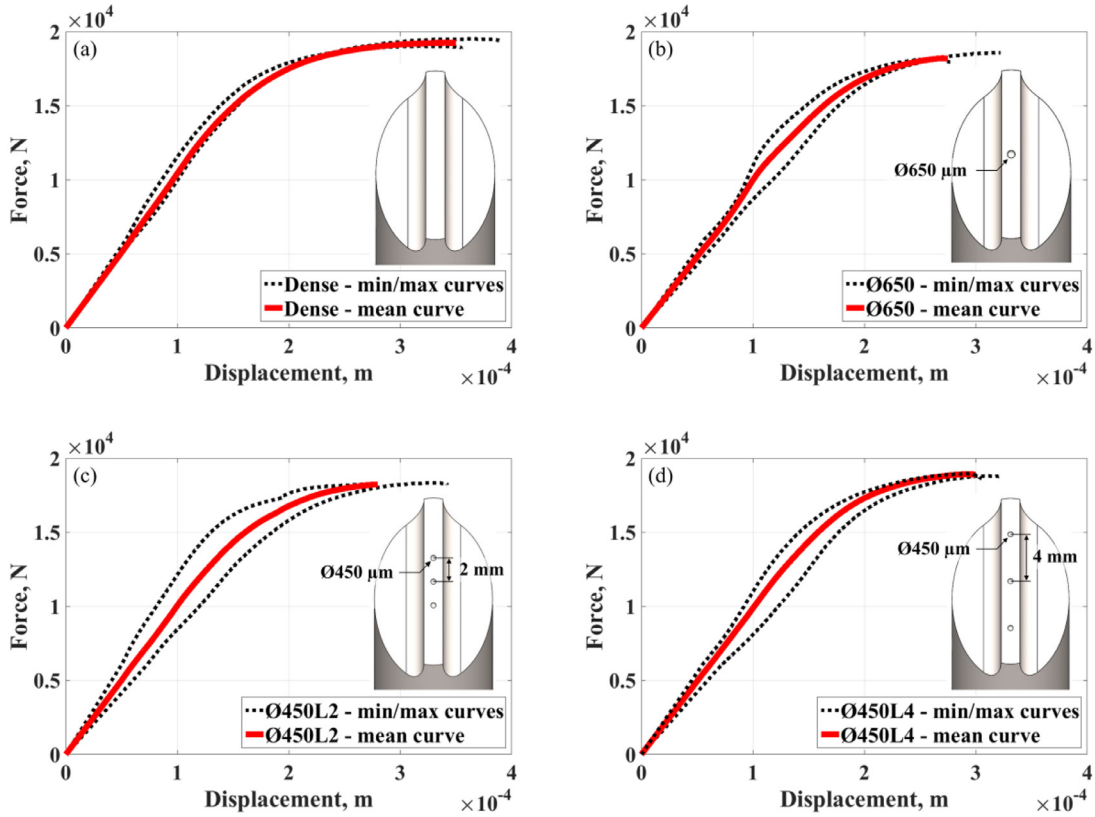


Fig. 7. Load-displacement curves of all specimens contains spherical pores (i.e., Ø650, Ø450L2 and Ø450L4), compared to dense specimens (i.e., without artificial pores). The red thick line represents the mean curve and the black dotted line represents the min/max curves.

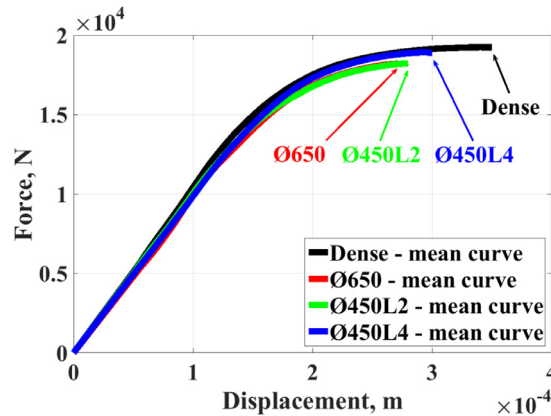


Fig. 8. Load-displacement mean curves of all specimens contains spherical pores compared to dense specimens, at nominal strain rate of $1 \times 10^{-4} \text{ s}^{-1}$.

3.3. Quasi-static tension of STS with prolate pores

Quasi-static tensile testing was performed to measure the load-displacement of specimen containing single prolate (elongated) spheroid. A set of 4 specimens of each type were tested in the same conditions as previously described for the quasi-static tests. Each specimen type contains prolate pore, which its major axis oriented at 4 different angles with respect to the mid-section of the inclined gauge i.e., 0° , 45° , 90° and 135° labelled as P0, 945, P90 and P135 respectively. Fig. 11 (a–d) shows the load-displacement results of the four specimen types. Fig. 12 summarizes the load-displacement results of the mean curves of all specimen types that presented in Fig. 11 (a–d), compared to the dense specimens mean curve. It can be observed that the pore orientation in the gauge section has no visible effect on the measured load-displacement curve.

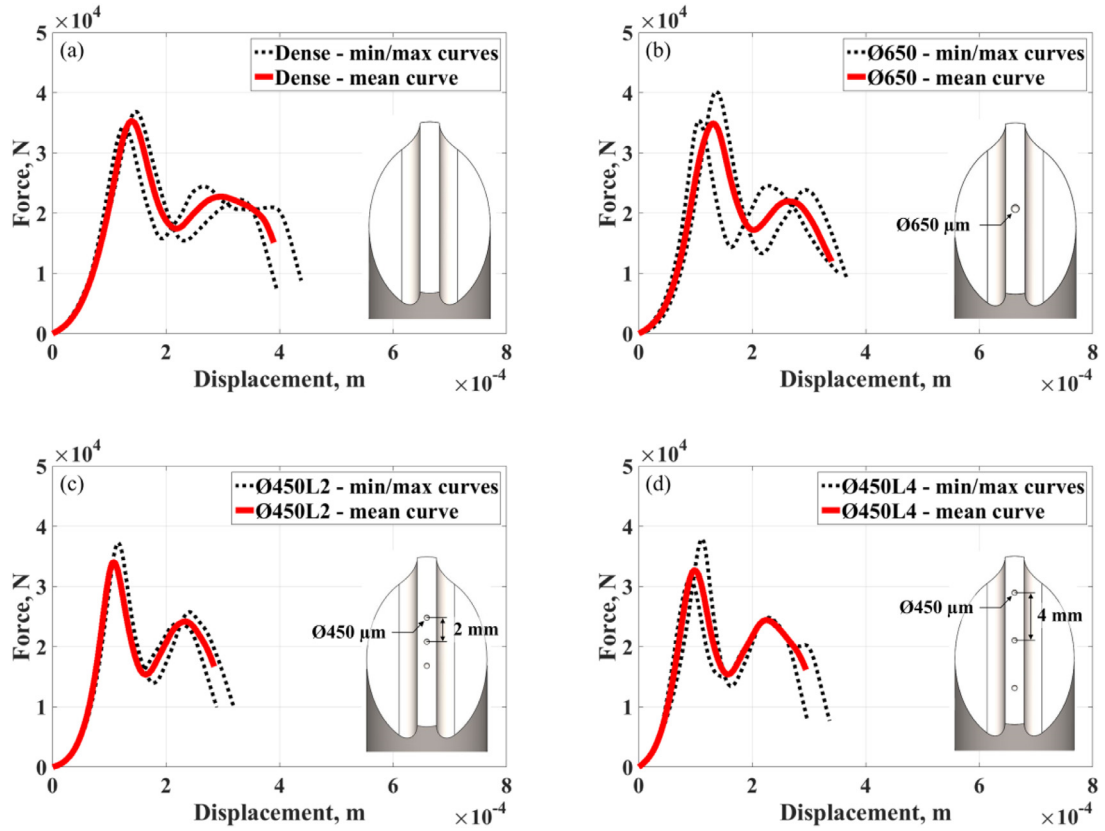


Fig. 9. Load-displacement curves of all specimens contains spherical pores (i.e., Ø650, Ø450L2 and Ø450L4), compared to dense specimens (i.e., without artificial pores). The red thick line represents the mean curve and the black dotted line represents the min/max curves.

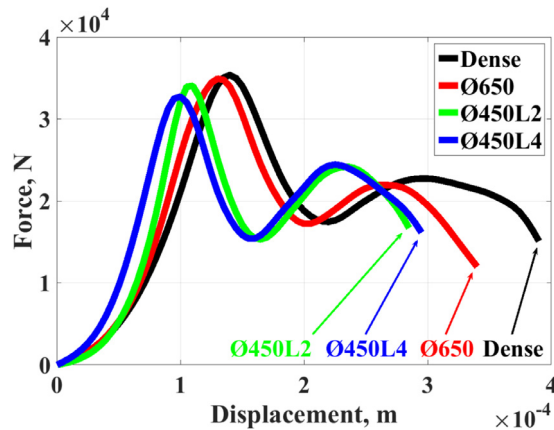


Fig. 10. Load-displacement mean curves of all specimens contains spherical pores compared to dense specimens, at nominal strain rate of approximately $1 \times 10^4 \text{ s}^{-1}$.

Again, the displacement to failure of the specimens containing prolate pore is smaller than that of the dense specimens while the differences in load are quite minor.

3.4. Dynamic tension of STS with prolate pores

The geometry of the specimens and pores arrangements in the dynamic tests is the same as for the quasi-static tests. A set of 5 specimens of each type were tested in the same conditions as previously described for the dynamic tests. Fig. 13 (a–d) shows the load-displacement results of the specimens containing prolate pore (i.e., P0, P45, P90 and P135). Fig. 14

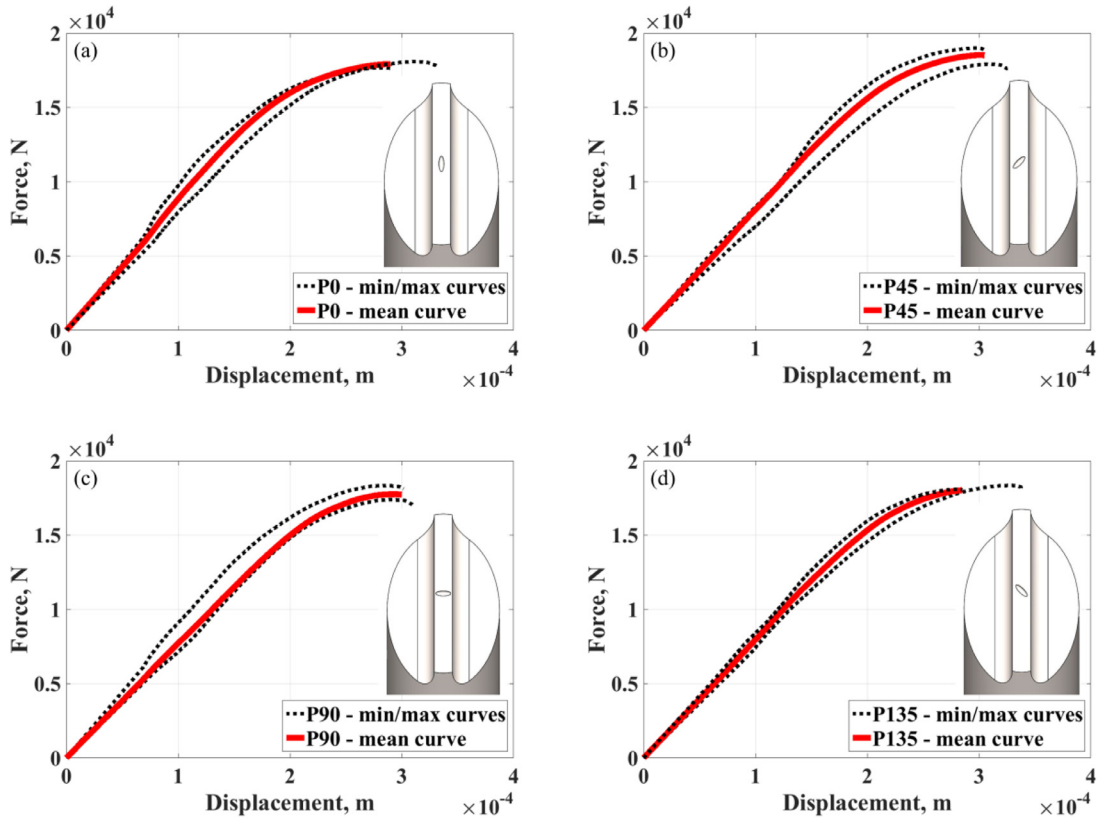


Fig. 11. Load-displacement curves of all specimens contains prolate pore (i.e., P0, P45, P90 and P135). The red thick line represents the mean curve and the black dotted line represents the min/max curves.

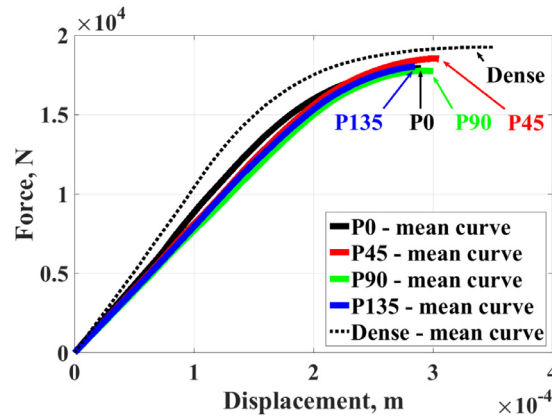


Fig. 12. Load-displacement mean curves of all specimens contains prolate pore compared to dense specimens, at nominal strain rate of $1 \times 10^{-4} \text{ s}^{-1}$.

summarizes the load-displacement results of the mean curves of all specimen types that presented in Fig. 13 (a–d), compared to the dense specimens mean curve. In the dynamic loading case too, one can observe that the orientation of the pore has no significant effect on the measured load-displacement curve. However, a reduction in the displacement to failure and load can be observed in specimens containing prolate pores compared to the dense specimens. Fig. 15 (a–b) shows a comparison between the results of specimens containing spherical and prolate pore at different strain rates. For the quasi-static tests, each curve represents the mean curve of all specimens containing spherical or prolate pore, 11 and 16 respectively. For the dynamic tests, each curve represents the mean curve of all specimens containing spherical or prolate pore, 14 and 19 respectively. Fig. 15 shows that at a fixed pore volume fraction, the shape of the pore (spherical or prolate) has no significant influence on the mechanical response, in both strain-rate regimes.

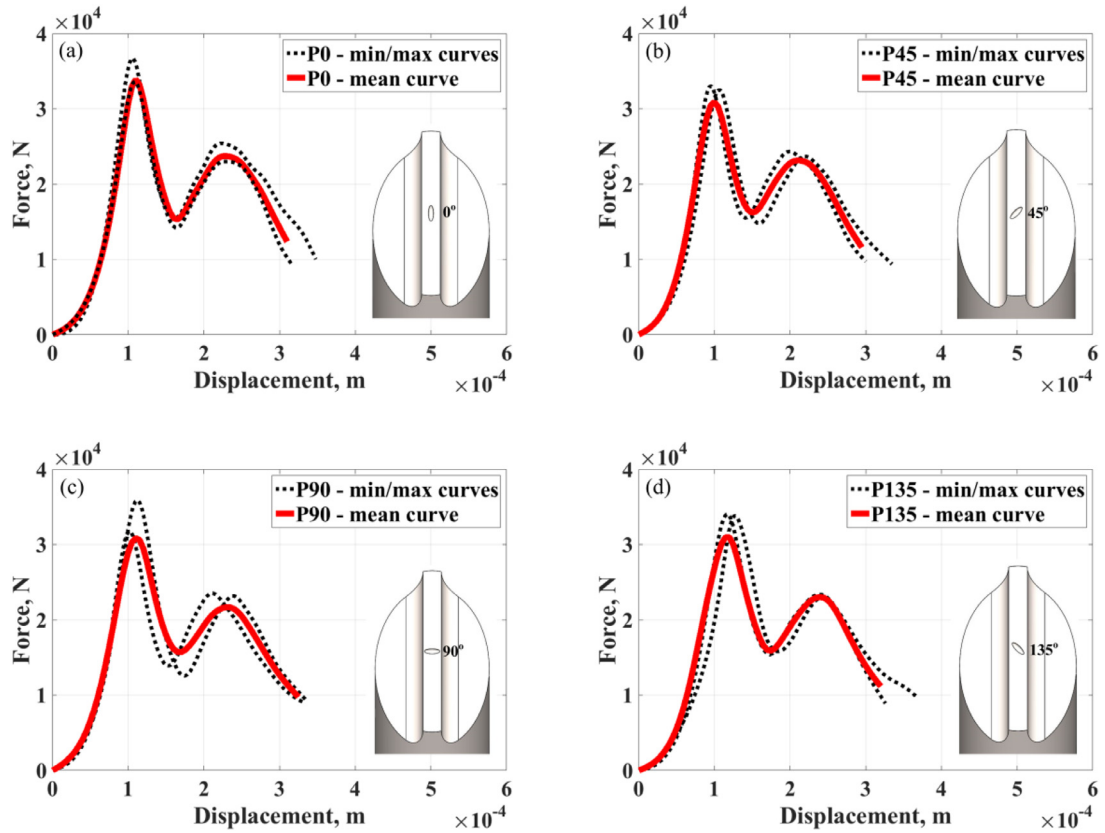


Fig. 13. Load-displacement curves of all specimens contains prolate pore (i.e., P0, P45, P90 and P135). The red thick line represents the mean curve and the black dotted line represents the min/max curves.

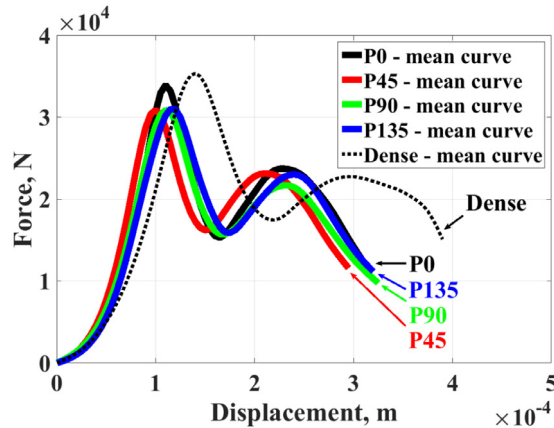


Fig. 14. Load-displacement mean curves of all specimens contains prolate pore compared to dense specimens, at nominal strain rate of approximately $1 \times 10^4 \text{ s}^{-1}$.

4. Discussion

The originality of this study lies on the investigation of embedded artificial voids in shear-tension specimens at different strain rates. For this purpose, this technology was found to be suitable, as it was demonstrated in previous studies for compression (Fadida et al., 2015) and tension (Fadida et al., 2018) of spherical voids. The experimental results are based on specific configurations of internal pores and under specific loading conditions. The volume fraction of the pores was kept constant in order to allow for comparison between the different configurations. However, the results are

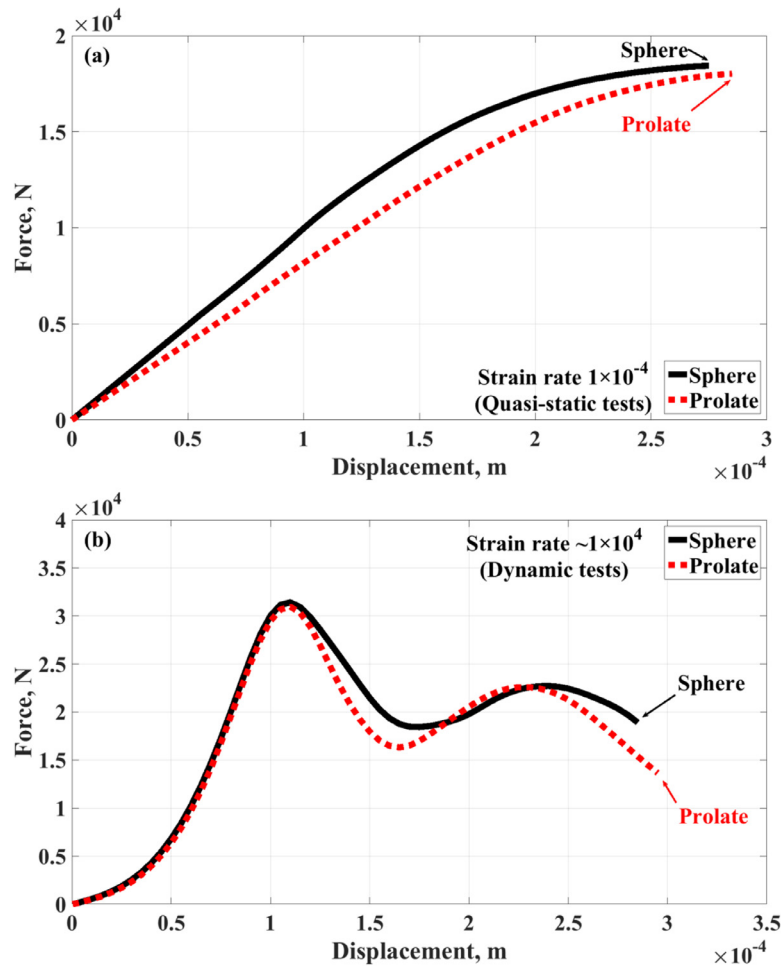


Fig. 15. A comparison between sphere and prolate pore embedded in shear-tension specimens at the geometric center of the gauge at different strain rates: $1 \times 10^{-4} \text{ s}^{-1}$ (a) and $\sim 1 \times 10^4 \text{ s}^{-1}$ (b).

not sufficient for straightforward generalization to any other configurations of pores or loading conditions. The results of shear-tension specimens containing discrete artificial pore (or pores) subjected to quasi-static and dynamic loading, shows that the presence of the pore has a noticeable effect on the mechanical response of the specimen. In both regimes, the displacement to failure of specimens containing pore (or pores) was smaller than that of the dense specimens, while a slight reduction in load was observed. Yet, the mechanical response of pore-containing specimens is quite similar to that of the dense specimens and the differences between their curves can only be observed at the final stage before rupture. These findings are quite consistent with those of Barsoum and Faleskog (2007a), that showed that the contribution of pre-existing voids to the onset of failure, under combined tension and shear loading, is quite minor. In both regimes, changing the distance between the spherical pores (i.e., 2 mm or 4 mm) did not result in a significant change of the load-displacement curves. Sevostianov, Kachanov, and Drach, (2014) showed that the effect of interactions on the elastic properties are quite weak. For instance, they found that shielding interaction effects remain noticeable at spacing between spheres of the order of three radii, which is relatively smaller than the *ratio* in the current study. Similarly, changes in the number of pores (i.e., one pore or three pores, whose total volume equals to the volume of the single pore), was not reflected in the tests results. The results of specimens containing prolate pore, shows that there is no sensitivity to the orientation of the pore in both regimes, for the specified spheroid and gauge dimensions. Spherical pore compared to prolate pore, which both has the same volume (but very differ in geometry), seem to cause a similar mechanical response, for both strain rates. The results shows that, the shape of the pore, the number of pores and their distribution do not play a significant role in dictating the failure in shear-dominated stress states. However, the presence of the pore (or pores), characterized solely by the predetermined value of void volume fraction (i.e., 0.15%), has a noticeable effect on the ductility to failure, but minor effect on load. The following Table 4 summarizes the key results of this study.

Table 4

A summary of the quasi-static and dynamic tests results. The symbols indicate the level of impact on the mechanical response, i.e., "+" for noticeable impact and "-" for minor impact.

| Parameters | Quasi-static | | Dynamic | |
|------------------------------|--------------|-------|---------|-------|
| | Load | Disp. | Load | Disp. |
| Presence of artificial pores | – | + | – | + |
| Distance between pores | – | – | – | – |
| Number of pores | – | – | – | – |
| Pore orientation | – | – | – | – |
| Pore shape | – | – | – | – |

5. Conclusions

In this study, artificial discrete pores were embedded in shear-tension specimens to explore the mechanical response in shear-dominated stress states, keeping the pore volume fraction constant. The conclusions are relevant to the specific void volume fraction of 0.15% and the configurations of pores that were predefined.

For both loading-rate regimes,

- The quantity of pores (one or three pores, whose total volume is equal to the volume of the single pore) seems to only have a minor effect on the overall mechanical response.
- The distance between spherical pores did not result in a significant change in mechanical response.
- The mechanical response of prolate-containing specimens is insensitive to the orientation of the pore.
- The shape of the pore, i.e., spherical or prolate does not seem to affect the mechanical response.
- Finally, the presence of the pores reduces the displacement to failure, compared to the dense specimens.

Acknowledgement

The authors wish to thank Dr. A. Dorogoy for his valuable technical assistance and discussions.

Supplementary materials

Supplementary material associated with this article can be found, in the online version, at doi:[10.1016/j.ijengsci.2019.05.003](https://doi.org/10.1016/j.ijengsci.2019.05.003).

Appendix

Numerical analyses were conducted using commercial finite element software Abaqus explicit 6.14-2 (ABAQUS 6.14, 2014). The aim of the analyses was to determine the strain rate of the STS within the gauge, which can be evaluated by a numerical-experimental procedure according to Dorogoy et al. (2016). The whole physical model of the shear-tension specimen, incident and transmitted bars was included in the numerical (finite element) model. The model was meshed with

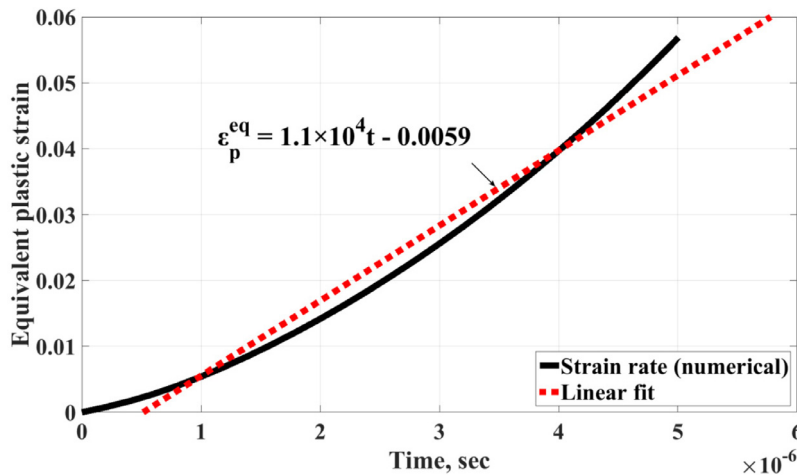


Fig. A1. The equivalent plastic strain at the mid-section versus time, which obtained from the numerical analysis.

linear hexahedral elements of type C3D8R with approximate size of 0.3 mm within the specimen's gauge and 3 mm along the bars. The initial input to describe the STS plastic behavior is according to a power law hardening material model (constitutive model), which its parameters were presented lately by Fadida et al. (2018). The strain rate was obtained by derivation of the numerical results for the equivalent plastic strain within the specimen's gauge, with respect to time. Fig. A.1 shows the average strain rate that was calculated by linear regression and found to be $1.1 \times 10^4 \text{ s}^{-1}$.

References

- ABAQUS 6.14. (2014). *ABAQUS/CAE 6.14-2 (2014)*. Providence, RI: Dassault Systèmes Simulia Corp.
- Andreau, O., Peyre, P., Penot, J. D., Koutiri, I., Dupuy, C., Pessard, E., et al. (2017). Deterministic defect generation in selective laser melting: Parametric optimization and control. In *Lasers manuf. - WLT eV* (pp. 1–11).
- Bao, Y., & Wierzbicki, T. (2004). A comparative study on various ductile crack formation criteria. *Journal of Engineering Materials and Technology Trans. ASME*, 126, 314–324. <https://doi.org/10.1115/1.1755244>.
- Barsoum, I., & Faleskog, J. (2007a). Rupture mechanisms in combined tension and shear-micromechanics. *International Journal of Solids and Structures*, 44. <https://doi.org/10.1016/j.jisolsolstr.2007.01.010>.
- Barsoum, I., & Faleskog, J. (2007b). Rupture mechanisms in combined tension and shear-experiments. *International Journal of Solids and Structures*, 44. <https://doi.org/10.1016/j.jisolsolstr.2006.09.031>.
- Becker, T. H., Beck, M., & Scheffer, C. (2015). Microstructure and mechanical properties of direct metal laser sintered Ti-6Al-4V. *South African Journal of Industrial Engineering*, 26, 1–10. <https://doi.org/10.7166/26-1-1022>.
- Beibei, H., Wenheng, W., Liang, Z., Lin, L., Qiyun, Y., Qianlei, L., et al. (2018). Microstructural characteristic and mechanical property of Ti6Al4V alloy fabricated by selective laser melting. *Vacuum*, 150. <https://doi.org/10.1016/j.vacuum.2018.01.026>.
- Benzerger, A. A. (2002). Micromechanics of coalescence in ductile fracture. *Journal of the Mechanics and Physics of Solids*, 50. [https://doi.org/10.1016/S0022-5096\(01\)00125-9](https://doi.org/10.1016/S0022-5096(01)00125-9).
- Biswas, N., Ding, J. L., Balla, V. K., Field, D. P., & Bandyopadhyay, A. (2012). Deformation and fracture behavior of laser processed dense and porous Ti6Al4V alloy under static and dynamic loading. *Materials Science and Engineering: A*, 549, 213–221. <https://doi.org/10.1016/j.msea.2012.04.036>.
- Blazynski, T. Z. (1987). *Materials at high strain rates* (p. 143). Netherlands: Springer.
- Bourcier, R. J., Koss, D. A., Smelser, R. E., & Richmond, O. (1986). The influence of porosity on the deformation and fracture of alloys. *Acta Metallurgica*, 34. [https://doi.org/10.1016/0001-6160\(86\)90147-1](https://doi.org/10.1016/0001-6160(86)90147-1).
- da Silva, M., & Ramesh, K. T. (1991). Effect of porosity on the plastic response of metals at high rates of deformation. In *Winter annual meeting of the American Society of Mechanical Engineers, December 1, 1991 - December 6* (pp. 105–118). Baltimore, United States: Publ by ASME, Johns Hopkins Univ.
- Danas, K., & Ponte Castaneda, P. (2012). Influence of the Lode parameter and the stress triaxiality on the failure of elasto-plastic porous materials. *International Journal of Solids Structures*, 49. <https://doi.org/10.1016/j.jisolsolstr.2012.02.006>.
- de Formanoir, C., Brulard, A., Vivès, S., Martin, G., Prima, F., Michotte, S., et al. (2017). A strategy to improve the work-hardening behavior of Ti-6Al-4V parts produced by additive manufacturing. *Materials Research Letters*, 5, 201–208.
- Dorogoy, A., & Rittel, D. (2017). Dynamic large strain characterization of tantalum using shear-compression and shear-tension testing. *Mechanics Materials*, 112. <https://doi.org/10.1016/j.mechmat.2017.06.003>.
- Dorogoy, A., & Rittel, D. (2005a). Numerical validation of the shear compression specimen. Part I: Quasi-static large strain testing. *Experimental Mechanics*, 45, 167–177. <https://doi.org/10.1177/0014485105052325>.
- Dorogoy, A., & Rittel, D. (2005b). Numerical validation of the shear compression specimen. Part II: Dynamic large strain testing. *Experimental Mechanics*, 45, 167–177. <https://doi.org/10.1177/0014485105052325>.
- Dorogoy, A., Rittel, D., & Godinger, A. (2016). A shear-tension specimen for large strain testing. *Experimental Mechanics*, 56. <https://doi.org/10.1007/s11340-015-0106-1>.
- Dorogoy, A., Rittel, D., & Godinger, A. (2015). Modification of the shear-compression specimen for large strain testing. *Experimental Mechanics*, 55. <https://doi.org/10.1007/s11340-015-0057-6>.
- EOS GmbH, (2004). Design Rules for DMLS - Application Notes [WWW Document]. URL <https://www.eos.info>
- Facchini, L., Magalini, E., Robotti, P., Molinari, A., Höges, S., & Wissenbach, K. (2010). Ductility of a Ti-6Al-4V alloy produced by selective laser melting of prealloyed powders. *Rapid Prototyping Journal*, 16, 450–459. <https://doi.org/10.1108/13552541011083371>.
- Fadida, R., Rittel, D., & Shirizly, A. (2015). Dynamic mechanical behavior of additively manufactured Ti6Al4V with controlled voids. *Journal of Applied Mechanics*, 82, 041004. <https://doi.org/10.1115/1.4029745>.
- Fadida, R., Shirizly, A., & Rittel, D. (2018). Dynamic tensile response of additively manufactured Ti6Al4V with embedded spherical pores. *Journal of Applied Mechanics Transactions ASME*, 85. <https://doi.org/10.1115/1.4039048>.
- George T. (Rusty), I. (2000). Classic split-Hopkinson pressure bar testing. In H. Kuhn, & D. Medlin (Eds.), *Mechanical testing and evaluation*. ASM International.
- Gologanu, M., Leblond, J.-B., & Devaux, J. (1993). Approximate models for ductile metals containing non-spherical voids. Case of axisymmetric prolate ellipsoidal cavities. *Journal of the Mechanics and Physics of Solids*, 41, 1723–1754. [https://doi.org/10.1016/0022-5096\(93\)90029-F](https://doi.org/10.1016/0022-5096(93)90029-F).
- Gurson, A. L. (1977). Continuum theory of ductile rupture by void nucleation and growth. I. Yield criteria and flow rules for porous ductile media. *Transactions of the ASME Series H, Journal of Engineering Materials and Technology*, 99, 2–15.
- Hancock, J. W., & Mackenzie, A. C. (1976). On the mechanisms of ductile failure in high-strength steels subjected to multi-axial stress-states. *Journal of the Mechanics and Physics of Solids*, 24. [https://doi.org/10.1016/0022-5096\(76\)90024-7](https://doi.org/10.1016/0022-5096(76)90024-7).
- Harding, J., Wood, E. O., & Campbell, J. D. (1960). Tensile testing of materials at impact rates of strain. *Journal of the Mechanical Engineering and Sciences*, 2, 88–96.
- Hutasoit, N., Masood, S. H., Pogula, K. S., Shuva, M. A. H., & Rhamdhani, M. A. (2018). Tensile properties of vacuum heat-treated Ti6Al4V alloy processed by selective laser melting. *IOP Conference Series: Materials Science and Engineering*, 377. <https://doi.org/10.1088/1757-899X/377/1/012138>.
- ISO/ASTM International. (2015). *ISO/ASTM 52900:2015 Additive manufacturing - general principles - terminology*. West Conshohocken, PA: ISO/ASTM International.
- Jones, D. R., Fensin, S. J., Diplo, O., Beal, R. A., Livescu, V., Martinez, D. T., et al. (2016). Spall fracture in additive manufactured Ti-6Al-4V. *Journal of Applied Physics*, 120. <https://doi.org/10.1063/1.4963279>.
- Kolsky, H. (1949). An investigation of the mechanical properties of materials at very high rates of loading. *Proceedings of the Physical Society*, 62, 676.
- Koplik, J., & Needleman, A. (1988). Void growth and coalescence in porous plastic solids. *International Journal of Solids and Structures*, 24. [https://doi.org/10.1016/0020-7683\(88\)90051-0](https://doi.org/10.1016/0020-7683(88)90051-0).
- Ladani, L., Razmi, J., & Choudhury, S. F. (2014). Mechanical anisotropy and strain rate dependency behavior of Ti6Al4V produced using E-beam additive fabrication. *Journal of Engineering Materials and Technology ASME*, 136. <https://doi.org/10.1115/1.4027729>.
- Li, Z., & Steinmann, P. (2006). RVE-based studies on the coupled effects of void size and void shape on yield behavior and void growth at micron scales. *International Journal of Plasticity*, 22, 1195–1216. <https://doi.org/10.1016/j.jplas.2005.07.004>.
- Machry, T., Eatock, D., Meyer, J., Antonyamy, A., Ho, A., & Prangnell, P. (2016). Effect of microstructure on the tensile strength of Ti6Al4V specimens manufactured using additive manufacturing electron beam process. *Powder Metallurgy*, 59. <https://doi.org/10.1080/00325899.2015.1123800>.
- Matthes, M., O'Toole, B., Trabia, M., Roy, S., Jennings, R., Bodenach, E., et al. (2017). Comparison of failure mechanisms due to shock propagation in forged, layered, and additive manufactured titanium alloy. In *Dynamic behavior of materials: 1* (pp. 131–138). Springer.

- McClintock, F. A. (1968). A criterion for ductile fracture by the growth of holes. *Journal of Applied Mechanics*, 35, 363–371.
- Moletsane, M. G., Krakhmalev, P., Kazantseva, N., du Plessis, A., Yadroitsava, I., & Yadroitsev, I. (2016). Tensile properties and microstructure of direct metal laser-sintered Ti6Al4V (ELI) alloy. *South African Journal of Industrial Engineering*, 27, 110–121. <https://doi.org/10.7166/27-3-1667>.
- Molinari, A., & Mercier, S. (2001). Micromechanical modelling of porous materials under dynamic loading. *Journal of the Mechanics and Physics of Solids*, 49(7), 1497–1516. [https://doi.org/10.1016/S0022-5096\(01\)00003-5](https://doi.org/10.1016/S0022-5096(01)00003-5).
- Nahshon, K., & Hutchinson, J. W. (2008). Modification of the Gurson Model for shear failure. *European Journal of Mechanics A/ Solids (France)*, 27, 1–17. <https://doi.org/10.1016/j.euromechsol.2007.08.002>.
- Nicholas, T. (1981). Tensile testing of materials at high rates of strain. *Experimental Mechanics*, 21. <https://doi.org/10.1007/BF02326644>.
- Nicholas, T. (1980). *Dynamic tensile testing of structural materials using a split Hopkinson bar apparatus*. Wright-Patterson AFB, OH: Air Force Wright Aeronautical Labs..
- Nielsen, K. L., Dahl, J., & Tvergaard, V. (2012). Collapse and coalescence of spherical voids subject to intense shearing: Studied in full 3D. *International Journal of Fracture*, 177. <https://doi.org/10.1007/s10704-012-9757-4>.
- Rice, J. R., & Tracey, D. M. (1969). On the ductile enlargement of voids in triaxial stress fields. *Journal of the Mechanics and Physics of Solids*, 17. [https://doi.org/10.1016/0022-5096\(69\)90033-7](https://doi.org/10.1016/0022-5096(69)90033-7).
- Rittel, D., Lee, S., & Ravichandran, G. (2002). A shear-compression specimen for large strain testing. *Experimental Mechanics*, 42. <https://doi.org/10.1007/BF02411052>.
- Rotbaum, Y., & Rittel, D. (2014). Is there an optimal gauge length for dynamic tensile specimens? *Experimental Mechanics*, 54. <https://doi.org/10.1007/s11340-014-9889-8>.
- Scheyvaerts, F., Onck, P. R., Tekoğlu, C., & Pardoën, T. (2011). The growth and coalescence of ellipsoidal voids in plane strain under combined shear and tension. *Journal of the Mechanics and Physics of Solids*, 59. <https://doi.org/10.1016/j.jmps.2010.10.003>.
- Sevostianov, I., & Kachanov, M. (2001). On the yield condition for anisotropic porous materials. *Materials Science and Engineering: A*, 313, 1–15. [https://doi.org/10.1016/S0921-5093\(01\)01215-1](https://doi.org/10.1016/S0921-5093(01)01215-1).
- Sevostianov, I., Kachanov, M., & Drach, B. (2014). On the effect of interactions of inhomogeneities on the overall elastic and conductive properties. *International Journal of Solids and Structures*, 51, 4531–4543. <https://doi.org/10.1016/j.ijsolstr.2014.08.029>.
- Tong, J., Bowen, C. R., Persson, J., & Plummer, A. (2017). Mechanical properties of titanium-based Ti-6Al-4V alloys manufactured by powder bed additive manufacture. *Journal of Materials Science & Technology (United Kingdom)*, 33, 138–148. <https://doi.org/10.1080/02670836.2016.1172787>.
- Tvergaard, V. (2008). Shear deformation of voids with contact modelled by internal pressure. *International Journal of Mechanical Sciences*, 50. <https://doi.org/10.1016/j.ijmecsci.2008.08.007>.
- Tvergaard, V. (1982). On localization in ductile materials containing spherical voids. *International Journal of Fracture (Netherlands)*, 18, 237–252.
- Wang, X., Xu, S., Zhou, S., Xu, W., Leary, M., Choong, P., et al. (2016). Topological design and additive manufacturing of porous metals for bone scaffolds and orthopaedic implants: A review. *Biomaterials*, 83, 127–141. <https://doi.org/10.1016/j.biomaterials.2016.01.012>.
- Wauthle, R., Ahmadi, S. M., Amin Yavari, S., Mulier, M., Zadpoor, A. A., Weinans, H., et al. (2015). Revival of pure titanium for dynamically loaded porous implants using additive manufacturing. *Materials Science and Engineering: C Materials Biological Applications*, 54. <https://doi.org/10.1016/j.msec.2015.05.001>.
- Weinong W. Chen, B. S. (2011). *Testing split Hopkinson (Kolsky) bar - design, testing and applications* (1st ed.). US: Springer <https://doi.org/10.1007/978-1-4419-7982-7>.
- Wilson-Heid, A. E., Novak, T. C., & Beese, A. M. (2018). Characterization of the effects of internal pores on tensile properties of additively manufactured austenitic stainless steel 316L. *Experimental Mechanics*. <https://doi.org/10.1007/s11340-018-00465-0>.
- Wulf, G. L. (1979). High strain rate compression of titanium and some titanium alloys. *International Journal of Mechanical Sciences (UK)*, 21, 713–718. [https://doi.org/10.1016/0020-7403\(79\)90051-1](https://doi.org/10.1016/0020-7403(79)90051-1).
- Xiaosheng, G., & Jinkook, K. (2006). Modeling of ductile fracture: Significance of void coalescence. *International Journal of Solids and Structures*, 43. <https://doi.org/10.1016/j.ijsolstr.2005.08.008>.
- Xiaosheng, G., Tingting, Z., Jun, Z., Graham, S. M., Hayden, M., & Roe, C. (2011). On stress-state dependent plasticity modeling: Significance of the hydrostatic stress, the third invariant of stress deviator and the non-associated flow rule. *International Journal of Plasticity*, 27. <https://doi.org/10.1016/j.ijplas.2010.05.004>.
- Zohdi, T. I., Kachanov, M., & Sevostianov, I. (2002). On perfectly plastic flow in porous material. *International Journal of Plasticity*, 18. [https://doi.org/10.1016/S0749-6419\(02\)00005-0](https://doi.org/10.1016/S0749-6419(02)00005-0).